3+1 dimensional integrated optics with localized light in a photonic band gap

Alongkarn Chutinan and Sajeev John

Department of Physics, University of Toronto, 60 St. George St., Toronto, Ontario, Canada, M5S 1A7

chutinan@physics.utoronto.ca, john@physics.utoronto.ca

Abstract: A general design for high-bandwidth, single-mode, lossless, optical micro-circuitry with fully three-dimensional circuit paths is demonstrated. Our 3D circuit design consists of dense stacking several planar microchip layers into the 2D-3D photonic band gap heterostructures and linking them with vertical interconnects. The 3D microchip enables an extra "dimension" of up to 200 nanometer single-mode wave-guiding in each planar chip layer and 100 nanometer bandwidth chip-to-chip interconnects in a variety of 3D PBG materials, including woodpile, slanted pores, and square spiral 3D PBG materials.

OCIS codes: (130.0130) Integrated optics, (130.2790) Guided waves, (130.3120) Integrated optics devices

References

1. S. John, "Electromagnetic absorption in a disordered medium near a photon mobility edge," Phys. Rev. Lett. **53,** 2169–2172 (1984).
2. S. John, "Strong localization of photons in certain disordered dielectric superlattices," Phys. Rev. Lett. **58,** 2486–2489 (1987).
3. D. Wiersma, P. Bartolini, A. Lagendijk, and R. Righini, "Localization of light in a disordered medium," Nature (London) **390,** 671–671 (1997).
4. E. Yablonovitch, "Inhibited spontaneous emission in solid-state physics and electronics," Phys. Rev. Lett. **58,** 2059–2062 (1987).
5. J. D. Joannopoulos, P. R. Villeneuve, and S. Fan, "Photonic crystals: Putting a new twist on light," Nature (London) **386,** 143–149 (1997).
6. C. M. Soukoulis, ed., *Photonic Crystals and Light Localization in the 21st Century* (Kluwer Academic, Dordrecht, 2001).
7. P. R. Villeneuve, S. Fan, and J. D. Joannopoulos, "Microcavities in Photonic Crystals: Mode Symmetry, Tunability and Coupling Efficiency," Phys. Rev. B **54,** 7837-8942 (1996).
8. A. Mekis, J. C. Chen, I. Kurland, S. Fan, P. R. Villeneuve, and J. D. Joannopoulos, "High transmission through sharp bends in photonic crystal waveguides," Phys. Rev. Lett. **77,** 3787–3790 (1996).
9. A. Chutinan and S. Noda, "Highly confined waveguides and waveguide bends in three-dimensional photonic crystal," Appl. Phys. Lett. **75,** 3739–3741 (1999).
10. M. M. Sigalas, R. Biswas, K. M. Ho, C. M. Soukoulis, D. Turner, B. Vasiliu, S. C. Kothari, and S. Lin, "Waveguide bends in three-dimensional layer-by-layer photonic bandgap materials," Microwave Opt. Technol. Lett. **23,** 56–59 (1999).
11. M. L. Povinelli, S. G. Johnson, S. Fan, and J. D. Joannopoulos, "Emulation of two-dimensional photonic crystal defect modes in a photonic crystal with a three-dimensional photonic band gap," Phys. Rev. B **64,** 075313 (2001).
12. D. Roundy, E. Lidorikis, and J. D. Joannopoulos, "Polarization-selective waveguide bends in a photonic crystal structure with layered square symmetry," J. Appl. Phys. **96,** 7750–7752 (2004).
13. S. Fan, P. R. Villeneuve, J. D. Joannopoulos, and H. A. Haus, "Channel Drop Tunneling through Localized States," Phys. Rev. Lett. **80,** 960–963 (1998).
14. M. Florescu and S. John, "Resonance fluorescence in photonic band gap waveguide architectures: Engineering the vacuum for all-optical switching," Phys. Rev. A **69,** 053810 (2004).

15. Z. Y. Li and K. M. Ho, "Waveguides in three-dimensional layer-by-layer photonic crystals," J. Opt. Soc. Am. B **20,** 801–809 (2003).
16. C. Sell, C. Christensen, J. Muehlmeier, G. Tuttle, Z. Y. Li and K. M. Ho, "Waveguide networks in three-dimensional layer-by-layer photonic crystals," Appl. Phys. Lett. **84,** 4605–4607 (2004).
17. A. Chutinan and S. John, "Light localization for broadband integrated optics in three dimensions," Phys. Rev. B **72,** 161316(R) (2005).
18. A. Chutinan, S. John, and O. Toader, "Diffractionless flow of light in all-optical microchips," Phys. Rev. Lett. **90,** 123901 (2003).
19. A. Chutinan and S. John, "Diffractionless flow of light in two- and three-dimensional photonic band gap heterostructures: Theory, design rules, and simulations," Phys. Rev. E **71,** 026605 (2005).
20. K. M. Ho, C. T. Chan, C. M. Soukoulis, R. Biswas, and M. Sigalas, "Photonic band gaps in three dimension: New layer- by- layer periodic structures," Solid State Comm. **89,** 413 (1994).
21. O. Toader, M. Berciu, and S. John, "Photonic band gaps based on tetragonal lattices of slanted pores," Phys. Rev. Lett. **90,** 233901 (2003).
22. O. Toader and S. John, "Slanted-pore photonic band-gap materials," Phys. Rev. E **71,** 036605 (2005).
23. R. Hillebrand, S. Senz, W. Hergert, and U. Gösele, "Macroporous-silicon-based three-dimensional photonic crystal with a large complete band gap," J. Appl. Phys. **94,** 2758–2760 (2003).
24. O. Toader and S. John, "Proposed square spiral microfabrication architecture for large three-dimensional photonic band gap crystals," Science **292,** 1133–1135 (2001).
25. O. Toader and S. John, "Square spiral photonic crystals: Robust architecture for microfabrication of materials with large three-dimensional photonic band gaps," Phys. Rev. E **66,** 016610 (2002).
26. K. M. Ho, C. T. Chan, and C. M. Soukoulis, "Photonic gaps for electromagnetic waves in periodic dielectric structures: Discovery of the diamond structure," in *Photonic Band Gaps and Localization,* C. M. Soukoulis, ed., (Plenum, New York, 1993).
27. K. S. Yee, "Numerical solution of initial boundary value problems involving Maxwell's equations in isotropic media," IEEE Trans. Antennas Propag. **14,** 302–307 (1966).
28. G. Mur, "Absorbing boundary conditions for the finite-difference approximation of the time-domain electromagnetic-field equations," IEEE Trans Electromagn. Compat. **EMC-23,** 377–382 (1981).
29. E. D. Palik, ed., *Handbook of Optical Constants of Solids* (Academic Press, Orlando, FL, 1985).
30. E. Yablonovitch, T. J. Gmitter, R. D. Meade, A. M. Rappe, K. D. Brommer, and J. D. Joannopoulos, "Donor and acceptor modes in photonic band structure," Phys. Rev. Lett. **67,** 3380–3383 (1991).
31. Strictly speaking, the two bands can be represented by two bases polarized in any two orthogonal directions in the *x-y* plane since they are doubly degenerate. However, it is more convenient to consider them as polarized along the *x-* and *y-* directions, respectively, as in the text.
32. C. Manolatou, S. G. Johnson, S. Fan, P. R. Villeneuve, H. A. Haus, and J. D. Joannopoulos, "High-density integrated optics," J. Lightwave Technol. **17,** 1682–1692 (1999).
33. J. Smajic, C. Hafner, and D. Erni, "Design and optimization of an achromatic photonic crystal bend," Opt. Exp. **11,** 1378–1384 (2003).
34. N. Moll and G. L. Bona, "Bend design for the low-group-velocity mode in photonic crystal-slab waveguides," Appl. Phys. Lett. **85,** 4322–4324 (2004).
35. J. S. Jensen and O. Sigmund, "Systematic design of photonic crystal structures using topology optimization: Low-loss waveguide bends," Appl. Phys. Lett. **84,** 2022–2024 (2004).
36. S. R. Kennedy, M. J. Brett, H. Miguez, O. Toader and S. John, "Optical properties of a three-dimensional silicon square spiral photonic crystal," Photonics and Nanostructures – Fundamentals and Applications **1,** 37–42 (2003).
37. M. O. Jensen and M. J. Brett, "Square spiral 3D photonic bandgap crystals at telecommunications frequencies," Opt. Exp. **13,** 3348–3354 (2005).
38. L. L. Seet, V. Mizeikis, S. Matsuo, S. Juodkazis, and H. Misawa, "Three-dimensional spiral-architecture photonic crystals obtained by direct laser writing," Adv. Mat. **17,** 541–545 (2005)
39. R. Z. Wang and S. John, "Engineering the electromagnetic vacuum for controlling light with light in a photonic-band-gap microchip," Phys. Rev. A **70,** 043805 (2004).
40. K. Iizuka, *Elements of Photonics* (Wiley-Interscience, New York, 2002).
41. M. Deubel, M. Wegener, A. Kaso, and S. John, "Direct laser writing and characterization of "Slanted Pore" photonic crystals," Appl. Phys. Lett. **85,** 1895–1897 (2004).
42. M. Deubel, G. von Freymann, M. Wegener, S. Pereira, K. Busch, and C. M. Soukoulis, "Direct laser writing of three-dimensional photonic-crystal templates for telecommunications," Nature Materials **3,** 444–447 (2004).
43. N. Tétreault, G. von Freymann, M. Deubel, M. Hermatschweiler, F. Perez-Willard, S. John, M. Wegener, and G. A. Ozin, "New Route to Three-Dimensional Photonic Bandgap Materials: Silicon Double Inversion of Polymer Templates," Adv. Mat. (in press).
44. M. Deubel, M. Wegener, S. Linden, G. von Freymann and S. John, "3D-2D-3D photonic crystal heterostructures by direct laser writing," (submitted to Optics Letters).

1. Introduction

A central goal of the fields of nano-electronics, plasmonics, and photonics is dense integration of information-processing components into a small volume. Inherently, electronic microchips operate on a single-channel flow of information and the device components are placed within a planar circuit board. Heat dissipation, cross-talk between circuit elements, and manufacturing cost are critical issues in the effort to reduce the size of electronic circuits toward the nanometer scale. In contrast, a photonic micro-chip offers simultaneous optical information flow through hundreds of wavelength channels without problems of cross-talk or heat dissipation. The main difficulty in conventional optical integrated circuitry is the inability to confine light within the optical circuit paths due to diffraction, scattering, and radiation losses. In general, this precludes the possibility of miniaturization of optical circuits to the sub-wavelength scales. In this paper, we present a robust and general solution to these fundamental problems using the principle of light localization in a photonic band gap (PBG) microchip.

Light localization [1, 2] is a fundamental optical phenomenon arising from strong resonant scattering and interference effects [3]. Photonic band gap (PBG) materials, a special class of photonic crystals (PC) [2, 4, 5], are artificial periodic dielectrics modulated on the scale of optical wavelengths. When a complete PBG exists, carefully engineered deviations from periodicity cause electromagnetic waves to interfere destructively in all but desired locations and directions, yielding localization or confinement of light into designed micro-cavities or waveguides. Light localization provides more robust confinement than the conventional refractive-index (total internal reflection) confinement. Most remarkably, the localization mechanism enables confinement of light in a low-index medium such as air. PBG materials provide a platform for optical microcircuits where a variety of optical components [6, 7, 8, 9, 10, 11, 12, 13, 14, 15, 16] including optical cavities, air-waveguides and waveguide bends, wavelength multiplexors, and optical switches, can be integrated on the wavelength scale, without diffraction losses. Recently, we have demonstrated a general design of fully three-dimensional integrated optics with single-mode air-waveguide circuit paths traversing the volume of a 3D optical microchip [17]. The design is a generalization of the two- and three-dimensional (2D-3D) PBG heterostructures, which provide a robust platform to intercalate a number of high-bandwidth planar 2D photonic crystal micro-circuit layers into a variety of 3D PBG materials [18, 19]. The 3D circuit design rules can be applied to provide high-bandwidth, lossless, optical links between planar micro-chips in various 3D PBG materials. The 3D microchip enables up to 200 nm single-mode waveguiding in each planar chip layer and 100 nm bandwidth chip-to-chip interconnects (for the center wavelength of 1.5 μm). This extra "dimension" of wavelength bandwidth allows a single circuit to simultaneously process hundreds of wavelength channels of information flow. The "3+1 dimensional" (3+1D) all-optical microchip enables an unprecedented speed and density of information flow and is broadly achievable in 3D PBG materials, regardless of architecture. In this paper, we illustrate these results with design rules and finite-difference time-domain (FDTD) simulation of light flow in three different 3D PBG architectures, namely, woodpile [20], slanted pore [21, 22, 23], and square spiral [24, 25] 3D PBG architectures.

Figure 1(a) shows a perspective view of our 3+1D micro-circuit. The paper is organized as follows. In Section 2, we briefly describe computational methods used in this paper. We begin consideration of the vertical waveguides that act as interconnects between two adjacent planar micro-circuit layers in Section 3. In particular, we show that a high-bandwidth, single-mode, air-waveguide in the vertical direction can be obtained by removing parts of dielectric, centered at the position where the field intensity peaks for certain photonic modes. In Section 4, the design of the 3+1D micro-circuit is described. A vertical 'U-turn' circuit path is formed by placing a vertical waveguide at the end of two in-plane waveguides of the adjacent planar microchip layers.
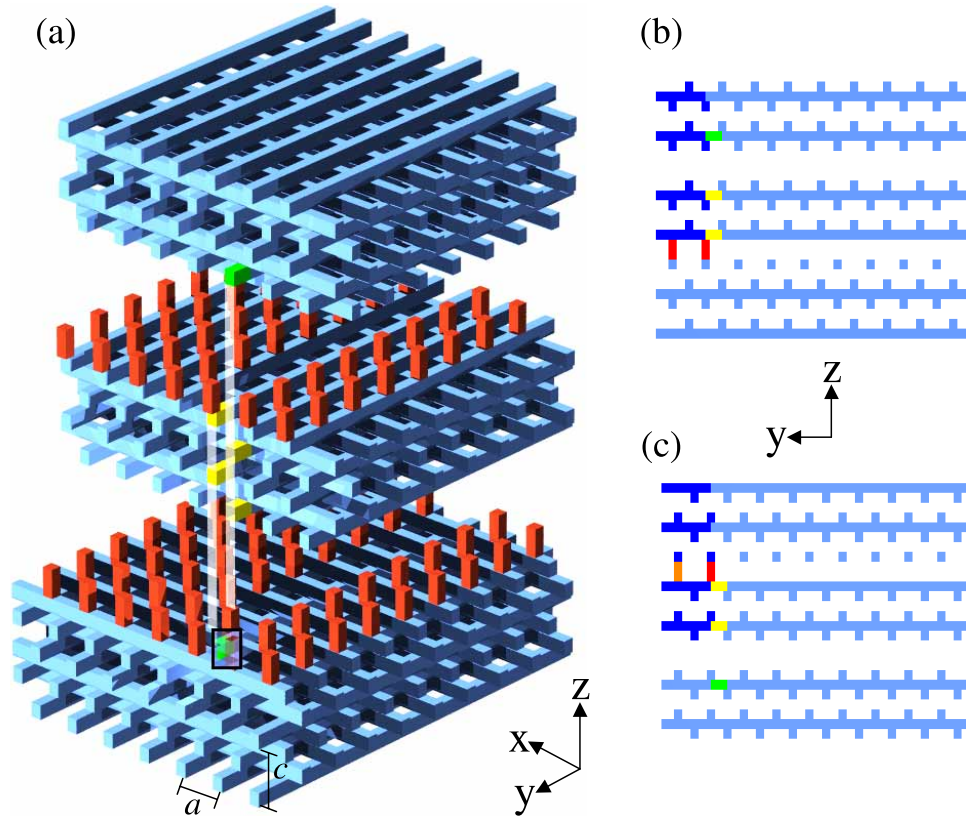
Fig. 1. Schematic of a 3+1D optical micro-chip for the woodpile 3D PBG architecture. The bottom, intermediate, and top cladding sections of the 3D micro-chip (consisting of the woodpile 3D PBG material) are separated to help visualize the 2D micro-chip layers (square lattice of red rods). The vertical waveguide is created by removing certain parts of dielectric rods along the *y*-direction marked by yellow and green (see text). A part of the bottom cladding section (inside the black wire frame) is made transparent to show end segment of the vertical waveguide (green) in (a). The transparent white strips are guides for the eyes. The *y*-*z* cross sections at the centers of the lower and upper 2D PC waveguides are shown in (b) and (c), respectively. The upper 2D PC waveguide is shifted to the +*x*-direction by 0.5*a* relative to the lower 2D PC waveguide. The orange rod in the upper 2D micro-chip layer in (c) and the dark blue woodpile rods in (b) and (c) are not shown in (a) for the sake of visualization of other features.

2. Computational methods

Two different numerical methods are used to investigate the properties of photonic crystal heterostructures. We employ the plane-wave (PW) expansion method [26] to obtain the band structures of the 3D PBG cladding layers. We use a supercell technique to calculate the band structures of the heterostructures. In our calculation, the unit cell is in a tetragonal lattice with an in-plane lattice constant, a, and a vertical lattice constant, c. A supercell with the size of $1 \times 1 \times 6$ unit cells is used to calculate the band structure of the heterostructure without any on-chip defects. In this case, approximately 1,800 plane waves are used to expand the electromagnetic (EM) field. The dispersion relation of the on-chip waveguide mode is calculated using a supercell with the size of $1 \times 6 \times 6$ unit cells, where up to 9,500 plane waves are used. The

Fourier transform of dielectric constant is calculated by fast Fourier transform (FFT) with resolution of 80 mesh points per a. We use the finite-difference time-domain (FDTD) [27] method to calculate the propagation of light inside the 3+1D circuits. A large FDTD computational domain with Mur's second-order absorbing boundary conditions (ABC) is used [28]. The spatial resolution of FDTD is 10 mesh points per a. In order to keep the resolution the same for the in-plane and vertical directions, we choose the vertical lattice constant c to be an integer multiple of $0.1a$. Furthermore, the four-fold screw symmetry about the vertical axis of the 3D PBG structures considered in this paper suggests that $c/4$ should be an integer multiple of $0.1a$. Here we consider only the cases where $c=1.2a$. We assume for all of the structures in this paper the dielectric constant of 11.9, corresponding to that of silicon at $1.5\,\mu$m [29].

3. Design of vertical waveguides

A single-mode, high-bandwidth, air waveguide can be obtained by introducing an appropriate line defect in the 3D photonic crystal. While there have been specific designs for in-plane, single-mode, high-bandwidth, air waveguides in 2D photonic crystals [8], 2D-3D photonic crystal heterostructures [18, 19], and the woodpile 3D photonic crystal [9], universal guidelines have not yet been elucidated for broadband 3D circuit paths in general photonic crystal
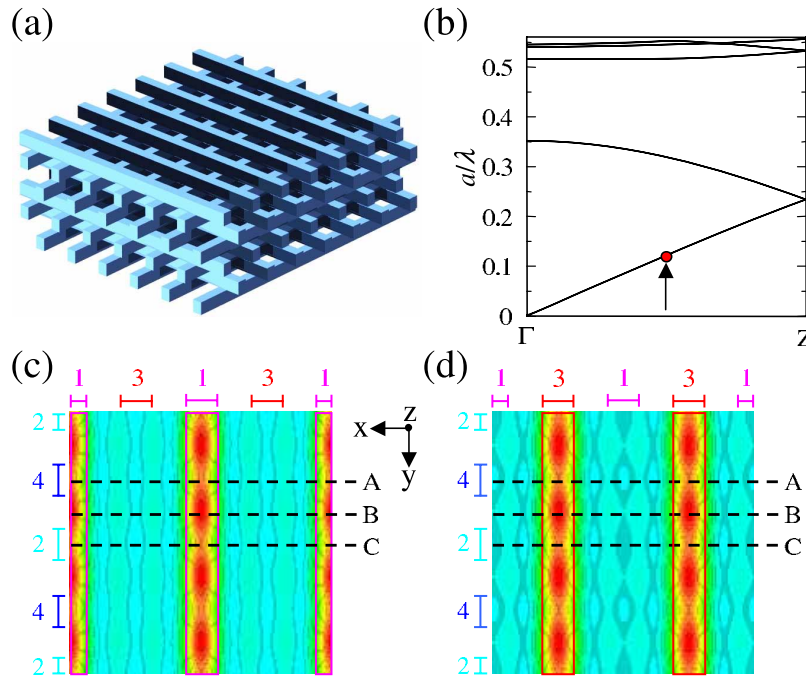

Fig. 2. (a) Schematic of the woodpile 3D PBG material. (b) Band structure for the woodpile structure using a tetragonal lattice for the Bloch vectors along the z-direction. There are two pairs of doubly degenerate bands below the PBG. The arrow points to the mode for which the electric displacement field distribution is shown in (c) and (d). This corresponds to the first band at the Bloch vector $0.25\,[2\pi/c]$. Large amplitudes of the y-component of electric displacement field in the x-y plane are shown as red shading at the center of the (c) first and (d) third layers. Except for the different envelope wave vector, the field pattern shown here is similar to that of the first band at the Z-point discussed in the text and Appendix. The numbers 1-4 denote the positions and stacking order of the woodpile layers.

structures. In this section, we demonstrate that simple and generally applicable guidelines exist even for complex 3D PBG architectures.

In general, the removal or addition of dielectric into photonic crystal structures creates defect modes inside the band gaps [30]. The design of functional defect modes is facilitated by careful examination of the electromagnetic field distributions of the perfect crystal near the proposed defects. For simplicity, we first consider the woodpile structure (depicted in Fig. 2(a)). Figure 2(b) shows the band structure of the woodpile using a tetragonal lattice (without defects) for the wave vectors along the z-direction. For the purpose of creating air waveguides, we only need to consider the bands below the PBG since only these bands are responsible for creation of any air defect modes inside the band gap. In Fig. 2(b), there are two pairs of doubly degenerate bands below the PBG. Careful examination of electric field patterns of all the four bands reveals that the lower two bands roughly correspond to the EM modes with the electric field polarized along the y- and x- directions [31], respectively, with the envelope wave vector equal to the Bloch wave vector. The higher two bands are similar to the lower two bands, except that they possess higher wave vector (frequency) component equal to $2\pi/c$. A simple analysis explains why all the four bands are degenerate at the Brillouin zone boundary (see Appendix for details). We show in Figs. 2(c), (d) the dominant (y-) component of the electric displacement field in the x-y plane at the center of the first layer and third layer, respectively, for the first band at the Bloch wave vector 0.25 $[2\pi/c]$. Beside that the electric field is polarized along and mainly confined inside the dielectric rods (y-direction), it is seen that the field amplitude is not uniform along the rods. The field is weak at positions that correspond to the centers of the rods in the adjacent layers (points A and C), and strong at positions in between (point B). We demonstrate that a vertical single-mode, high-bandwidth, air waveguide can be obtained by removing dielectric centered at the peak (point B). The removed part can extend to the nodes (points A and C). The removal should be done for both the first and third layers since the field resides in both layers and should be repeated for each unit cell along the vertical waveguide.

We show in Fig. 3(a) a schematic for the air waveguide with removed parts along the y-direction of length $0.5a$. In Fig. 3(b), we show the corresponding waveguiding band structure. The waveguide mode spans a normalized frequency range of a/λ=0.380-0.417. This corresponds to a single-mode waveguiding bandwidth of $\sim$147 nm near the wavelength of 1.5 μm
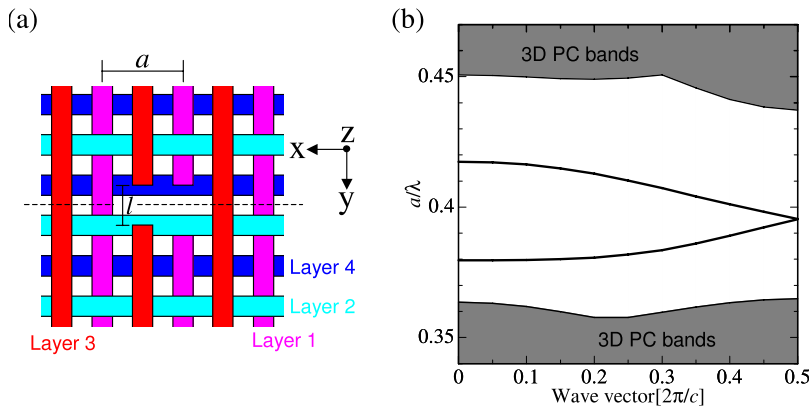

(a)   (b)

Fig. 3. (a) Schematic of the vertical waveguide in the woodpile. Parts of dielectric rods with the length l are removed from the first and third layers in each unit cell along the z-direction. (b) Dispersion relation for the vertical waveguide consisting of the zig-zag pattern of the removed dielectric rods of length l=0.5a. A single waveguide mode spans the frequency range a/λ=0.380-0.417.

when a is ~600 nm. Note that the dispersion curves of the waveguide mode consist of two bands, corresponding to their origins, the first and third bands of the periodic structure. The degeneracy at the Brillouin zone boundary is also conserved for this waveguide structure. Empirically, we find that the air waveguide mode created will have the same polarization as the original bands. In this case, the electric field is polarized along the y-direction. Similarly, by symmetry, removing dielectric from the second and fourth layers (consisting of rods parallel to the x-direction) creates a vertical waveguide with electric fields polarized along the x-direction.

4. 3+1 dimensional micro-circuits of light

There are many ways to form a 3D circuit path by connecting two planar micro-circuit layers with the vertical waveguide. Available options include relative positions and directions between two waveguides in the lower and upper micro-circuit layers, distance between the lower and upper micro-circuit layers, positions of the vertical waveguide, and polarization of the vertical waveguide modes. Here, we apply a simple consideration on the polarization of guided modes to obtain high bandwidth transmission through three-dimensional circuit bends. In particular, we argue that in order to create efficient (non-reflecting) waveguide bends, the direction of either the electric or magnetic field is conserved as light traverses the bend. For example, waveguide bends connecting two TM (TE) waveguides are efficient because the direction of electric (magnetic) field vector is conserved. In this case, the electric (magnetic) field vector of the incoming waveguide is matched with that of the outgoing waveguide so that it can *excite* the outgoing field efficiently. However, waveguide bends connecting a TE waveguide to a TM waveguide exhibit poor transmission characteristics. In this case, neither the electric nor magnetic field vector is matched for the incoming and outgoing waveguide so that efficient energy transfer is not possible.

We now consider a 3D circuit path (see Fig. 1(a)). Assume the incoming waveguide in the lower 2D micro-chip layer propagates light along the y-direction. Since the polarization of the 2D photonic crystal waveguide is predominantly TM-like (magnetic field is along the x-direction), the vertical waveguide requires a matching magnetic field along the x-direction. In this case, a vertical waveguide is created by removing parts of the dielectric rods along the y-direction. Similar consideration connecting the vertical waveguide to the outgoing waveguide in the upper 2D micro-chip layer requires that the outgoing waveguide in the upper 2D micro-chip layer is also along the y-direction. There are two interconnect options between the two micro-chip layers. The first option is a vertical U-turn circuit path, consisting of forward propagation of light on the lower 2D microchip waveguide followed by a 90° turn upward along a vertical interconnect and then another 90° turn backward on the upper micro-chip layer (forward-upward-backward). The second option is a forward-upward-forward circuit path. We illustrate the principles of 3D PBG circuit design for the 'U-turn' case. Similar considerations apply to the second option. More complex guiding options involving consecutive waveguide segments spanning all three spatial directions (see. Fig. 4) can be achieved by combining the U-turn bend with an in-plane bend.

4.1. Woodpile based 3+1D circuits

In the woodpile-based 2D-3D heterostructure shown in Fig. 1, the bottom cladding section consists of four or more unit cells (in depth) of the woodpile 3D PBG materials. One layer of the woodpile structure contains parallel rectangular rods with width and height of $0.25a$ and $0.3a$, respectively, where a is the distance between two adjacent rods in the same layer. As one unit cell of the woodpile contains four stacking layers, the periodicity in the stacking (vertical) direction is $c=1.2a$. The lowest planar micro-chip layer, sitting on the bottom cladding section, consists of a square lattice (lattice constant also equal to a) of square rods with the matching

width of $0.25a$. The thickness of each 2D PC layer is $0.6a$. The lowest planar circuit layer is separated from the next planar circuit layer by at least 3 unit cells (in depth) of the woodpile structure (only 1.75 unit cells are shown in Fig. 1). The second planar circuit layer is stacked on top of the 3D PBG separator section and the same process can be repeated to intercalate as many planar microchips as desired. The separator sections and top cladding section are laterally aligned with the bottom cladding sections as follows: If the 2D micro-chip layers were removed and 3D PBG cladding sections were re-connected by vertical displacement, a bulk woodpile structure would be reconstituted. In the lowest 2D micro-chip layer, one rod is placed at each of the square lattice points defined by crossing points of the topmost woodpile layer of the bottom cladding section and the bottommost woodpile layer of the separator section. The lateral position for any other 2D PC layers is also defined in a similar way.

A waveguide in the lower planar micro-chip layer is created by removing a row of dielectric rods along the y-direction of the square lattice. The vertical waveguide, acting as an interconnect between the lower and upper planar micro-chip layers, is placed next to the end of the lower layer waveguide as shown in Fig. 1. As discussed above, the vertical waveguide is created by removing parts from dielectric rods along the y-direction. Finally, a 2D photonic crystal waveguide is created along the $(-y)$-direction in the upper planar micro-chip layer to form a U-turn circuit path. For the current design, the single-mode bandwidth is ($a/\lambda \sim 0.364$-0.411), 185 nm for the in-plane waveguide and ($a/\lambda \sim 0.380$-0.417), 147 nm for the vertical interconnect. The overlap bandwidth of $a/\lambda \sim 0.380$-0.411 represents the overall single-mode bandwidth of the 3D circuit path. For a U-turn, the four-fold screw symmetry about the z-axis of the woodpile structure [20] (like the square spiral photonic crystal [24] and the slanted pore $\mathbf{SP_2}$ [21]), requires that the number of the woodpile layers in the separator section is equal to $4n+3$, where n is an integer. A U-turn in the separator section consists of climbing three out of four segments of the screw within a single unit cell. This imposes a $0.5a$ lateral shift in the upper air waveguide relative to the lower waveguide. Our design rule for the vertical interconnect consists of removing dielectric from the 3D PBG separator section within the boxes shown in yellow in Fig. 1. Notice that the woodpile layers in the separator that are adjacent to the 2D micro-chip layers have parts of their dielectric rods removed to create the vertical waveguide. To eliminate cross-talk between the adjacent 2D micro-chip layers we use a separator section with thickness of 15 woodpile layers (or 3.75 unit cells).

We use the finite-difference time-domain method (FDTD) to calculate the transmission and reflection spectra of the U-turn optical interconnect. This vertical interconnect acts as a structurally symmetric Fabry-Perot cavity (with three resonant frequencies where the transmission reaches 100% as expected from mode coupling theory [32]) in the circuit path defined by the U-turn. The off-resonant transmission, however, is determined by the quality (Q) factor of the cavity and is low when the Q factor of the cavity is high. For a high Q factor vertical interconnect, consisting of dielectric removed only from the yellow boxes shown in Fig. 1, the transmission drops to 30-55% at the off-resonant frequencies. In order to obtain uniformly high transmission around the U-turn, it is necessary to lower the Q factor of the vertical interconnect [32]. The key step to eliminate backscattering at the vertical waveguide bend is the removal of additional dielectric from the top and bottom woodpile cladding sections throughout the green boxes depicted in Fig. 1. This extension of the vertical waveguide above and below the 2D micro-chip layers is a simple and effective mechanism for achieving large bandwidth chip-to-chip interconnection in PBG materials. The final structure exhibits a high transmission for the U-turn over the frequency range $a/\lambda \sim 0.381$-0.403 (corresponding to a bandwidth of $\sim$90 nm near 1.5 μm), as shown by solid lines in the inset of Fig. 4. It is likely that further refinement [33, 34, 35] of the vertical elbow design would improve the transmission characteristics even further. Note that the upper limit of the waveguiding bandwidth of the U-turn circuit path shown
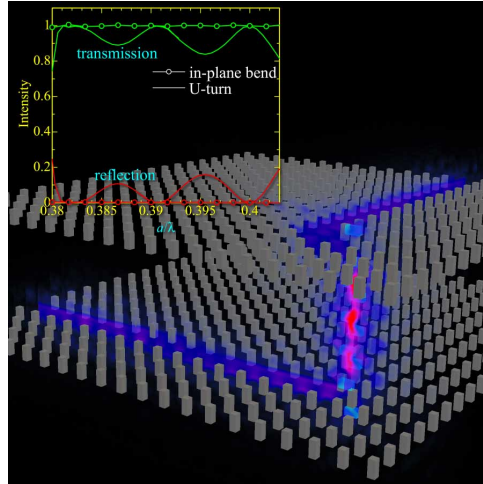
Fig. 4. Time-averaged electric field intensity for the woodpile based circuit with both in-plane and vertical bends at the frequency a/λ=0.39. An inset shows transmission and reflection spectra for the U-turn (solid lines) and the in-plane 90° bend (solid lines with circles).

in the inset of Fig. 4 (a/λ=∼0.403) does not reach the upper cut-off frequency of a/λ=0.411 (see previous text). We attribute this to the slow group velocity of the 2D photonic crystal waveguide near the cut-off.

More complex circuit paths are easily obtained by combining the vertical U-turn interconnect with other in-plane waveguide apertures. A simple non-planar circuit path (depicted in Fig. 4) is obtained by combining the vertical U-turn with an in-plane 90° bend. The transmission and reflection spectra for the 90° bend in the 2D micro-chip layer is shown in the inset of Fig. 4 (solid lines with circles), where almost 100% transmission is obtained over the entire range of frequency [19]. Figure 4 shows the time-averaged field intensity for the circuit with both in-plane and vertical bends at the frequency a/λ=0.39.

While the woodpile structure lends itself very naturally to wave-guide and 3D-circuit design as described above, the same principles of design apply to much more complex 3D PBG architectures. In this regard, we further illustrate the generality of 3D PBG circuit design using the slanted pore and square spiral architectures. Remarkably the slanted pore architecture provides even better optical transmission characteristics than the woodpile.

4.2. Slanted pore 3D PBG based 3+1D circuits

As mentioned above, similar design rules can be applied to 2D-3D heterostructures based on other types of 3D PBG materials. Here we describe results for a 3+1D circuit using the Slanted Pore 3D PBG [21] based heterostructure. In particular, we consider the so-called SP_2 structure, where two slanted pores are drilled in each unit cell of the square lattice. The SP_2 crystals are defined by a tetragonal lattice with lattice constants c along the z axis and a along the x and y axes (see Fig. 5(a)). One unit cell consists of two cylindrical pores of radius r aligned along the $(0, 0, 0)$-(a, a, c) and $(0.5a, 0, 0)$-$(-0.5a, -a, c)$ directions. These two pores are displaced in the x-direction by $0.5a$. The SP_2 structure used here has the structural parameters c=1.2a and r=0.28a and exhibits a complete PBG of ∼17% (depicted in Fig. 5(b)). The dielectric volume fraction is roughly 34%. The lower 2D micro-chip layer is inserted at the plane z=1/8c, where the cross-section resembles a square lattice of dielectric islands in an air background (see the top surface
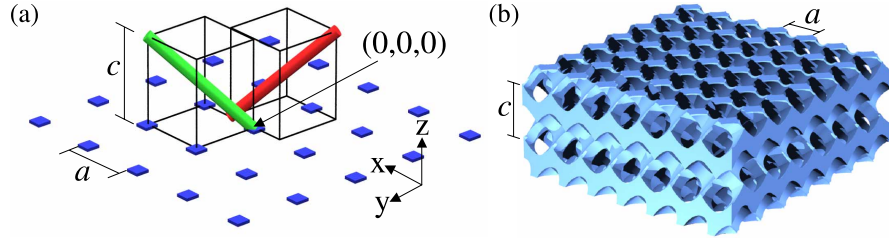
Fig. 5. (a) Schematic for the **SP₂** PBG architecture depicting two slanted pores drilled in each unit cell of the square lattice. (b) The **SP₂** structure with structural parameters $c=1.2a$ and $r=0.28a$. The top surface shows the plane $z=(1/8)c$.
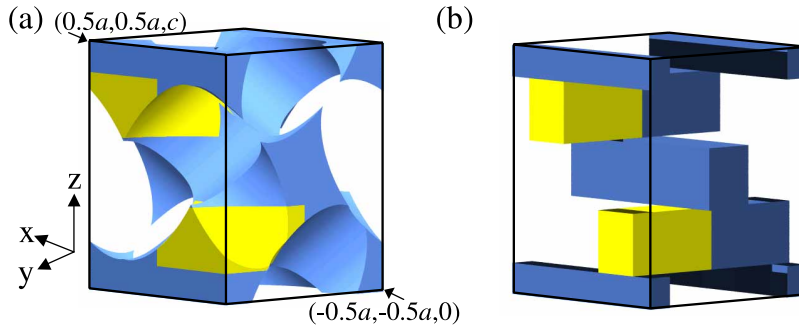

Fig. 6. Schematics of the unit cell of (a) the **SP₂** PBG architecture and (b) the woodpile PBG structure. The vertical waveguide for each structure is created by removing parts of dielectric marked by yellow in each of (a) and (b). The zig-zag pattern of removed dielectric is a common feature of both waveguides.

of Fig. 5(b)). This is common in a 2D-3D PBG heterostructure design [19]. One cylindrical rod is placed at each of the square lattice points, with one of them centered at $(-0.25a, 0.5a, 1/8c)$ (corresponding to the center of one of the dielectric islands). The thickness of the 2D PC layer is $0.6a$. The simplest way to visualize the 3D circuit architecture for the **SP₂** is by noting the similarity between the unit cell of the **SP₂** and that of the woodpile structure. Figures 6(a), (b) depict the **SP₂** unit cell as defined by the above coordinates and the corresponding woodpile unit cell, respectively. The vertical waveguide of the **SP₂** is created by removing dielectric inside the rectangular boxes defined by $(-0.5a, 0, 1/8c)$-$(0, 0.5a, 3/8c)$ and $(0, 0, 5/8c)$-$(0.5a, 0.5a, 7/8c)$, as indicated by yellow. The corresponding vertical waveguide for the woodpile is also indicated by yellow in the woodpile unit cell for comparison. There is a noticeable correspondence between the two 3D PBG structures. The entire 3D circuit architecture can be obtained by substituting the **SP₂** unit cells into the previously discussed woodpile 3D circuit. Figure 7 illustrates the final 3D circuit architecture for the **SP₂** with three micro-chip layers.

We again consider the U-turn structure for the **SP₂** based circuits. The transmission and reflection spectra for the U-turn over a distance of $d=3.75c$ (equivalent to 15 woodpile layers) are shown in Fig. 8 (red lines). A very high transmission of $> 94\%$ over a bandwidth of ~100 nm is obtained. This implies that the Q factor for the vertical waveguide cavity is very small in this case. We also show the transmission and reflection spectra for $d=7.75c$ (equivalent to 31 woodpile layers) in Fig. 8 (black lines). It is seen that there are more peaks in the transmission spectrum, indicating existence of more resonant frequencies. Higher reflections at peaks reveal that the Q factors increase with the increasing thickness of the separator layer. Nevertheless, the
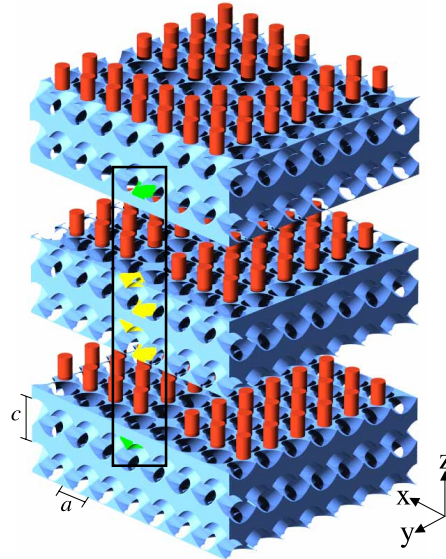
Fig. 7. Schematic of the 3+1D optical micro-chip using the **SP₂** 3D PBG architecture. The bottom, second, and third cladding sections of the micro-chip (consisting of the **SP₂** 3D PBG material) are separated to help visualize the 2D micro-chip layers. (The topmost cladding section is not shown). The vertical waveguide, connecting the bottom and the second micro-chip layers, is created by removing certain parts of dielectric rods along the *y*-direction marked by yellow and green (corresponding to the U-turn interconnect of the woodpile based 3+1D circuits shown in Fig. 1(a)). The left surface showing the vertical waveguide (highlighted by black wire frame) corresponds to the cross-section *y*=0.5*a* (see Fig. 6(a)).

high transmission of > 90% is maintained throughout the entire bandwidth. Finally, the blue lines in Fig. 8 indicate the transmission and reflection spectra for 90° bends in the 2D PC layer, where again almost 100% transmission is obtained over the same bandwidth.

4.3. Square spiral 3D PBG based 3+1D circuits

Finally, we show a 3+1D circuit using the Square Spiral 3D PBG [24, 25, 36, 37, 38] based heterostructure. Figure 9(a) illustrates the architecture of the square spiral structure. The square spiral structure consists of square spiral posts in a tetragonal lattice, with lattice constant *c* along the *z* axis and *a* along the *x* and *y* axes. The building block of the crystal is made from a coil of pitch *c* with a single loop whose transverse cross section is a square with sides of length *L*. The pitch is the same as lattice constant in the *z*-direction, and the coil is wrapped around the *z* axis. Each segment of the coil is coated with a cylinder of radius *r*. The structure considered here belongs to a group denoted as inverse [001]-diamond:5 [25], with structural parameters $[L, c, r]$ = [1.5, 1.2, 0.27]*a*, where the square spiral posts are made of air and embedded in a dielectric background. A schematic is shown in Fig. 9(b).

We define a coordinate system by centering one coil at the origin and assume that it is created by joining 5 points by 4 straight lines as follows (*L*/2, -*L*/2, 0)→(*L*/2, *L*/2, *c*/4)→(-*L*/2, *L*/2, *c*/2)→(-*L*/2, -*L*/2, 3/4*c*)→(*L*/2, -*L*/2, *c*). Figure 10(a) shows a unit cell of the square spiral that corresponds to that of the **SP₂** and woodpile shown in Fig. 6. The 3D circuit architecture for the inverse square spiral is shown in Fig. 11. Again, the lower 2D micro-chip layer is inserted at the plane where the cross-section of the lower 3D PBG cladding section represents a square lattice
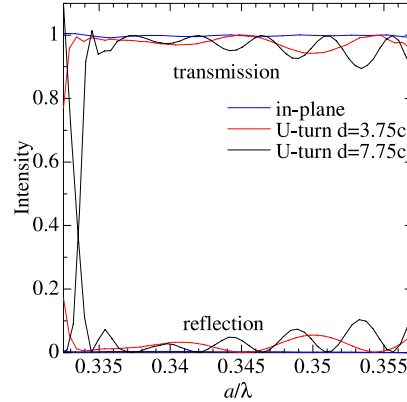
Fig. 8. Transmission and reflection spectra for two different vertical U-turn bends in the **SP₂** based 3D circuits, the first with a vertical interconnect of length $3.75c$ (red) and the second with length $7.75c$ (black). The corresponding spectra for a simple $90°$ in-plane bend are superimposed (blue).
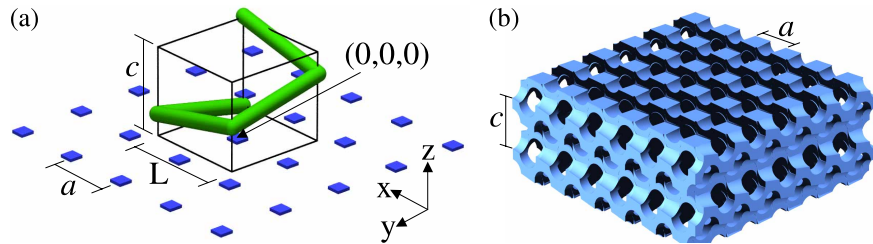

Fig. 9. (a) Schematic for the square spiral depicting a coil in each unit cell of the square lattice. (b) The inverse diamond:5 structure with structural parameters $c=1.2a$ and $r=0.28a$. The top surface shows the plane $z=0$.

of dielectric islands in an air background. In the case of the square spirals, this corresponds to the plane that cuts the spiral posts at the elbow or equivalently the plane $z=0$ (shown by the top surface of Fig. 9(b)). One rod is placed at each of the square lattice points, with one of them centered at $(0.25a, -0.25a, 0)$ (corresponding to the center of one of the dielectric islands). The radius and height of dielectric rods in the 2D micro-chip layers are $0.18a$ and $0.6a$, respectively. The vertical waveguide of the square spiral is also created in the same way as previous structures, by removing dielectric inside the rectangular boxes defined by $(0, 0.3a, 0)$-$(0.5a, 0.7a, 1/4c)$ and $(0.5a, 0.3a, 1/2c)$-$(a, 0.7a, 3/4c)$, as indicated by yellow in Fig. 10(a). Note that, unlike the woodpile, we choose the width of the vertical waveguide (along the y-direction) to be $0.4a$ instead of $0.5a$ since it gives better coupling between the in-plane and vertical waveguides. This vertical interconnect yields high transmission over a bandwidth of $\sim$95 nm for the U-turn in the square spiral based circuits, as shown in Fig. 10(b). The distance of $3.75c$ between two micro-chip layers is assumed in the calculation. Note that the transmission of more than unity near $a/\lambda=0.384$ is an artifact of the computational method [8, 9, 19].

5. Discussion

We have demonstrated a simple and unified design for high-bandwidth, single-mode, lossless, optical micro-circuitry with fully three-dimensional circuit paths, broadly applicable in a variety of 3D PBG architectures. We have illustrated the design principles using woodpile, slanted
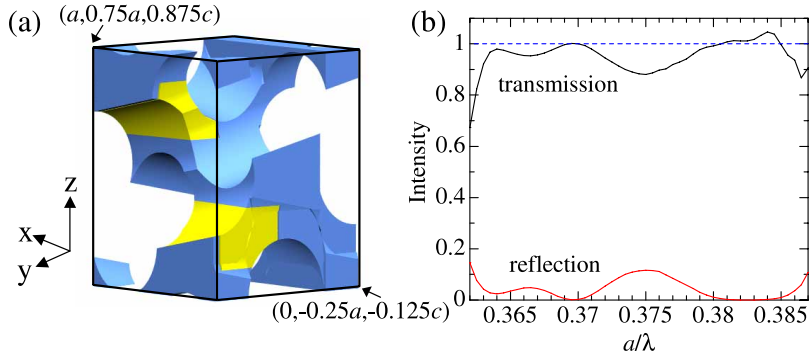
Fig. 10. (a) Schematic of the unit cell of the square spiral structure. The vertical waveguide is created by removing a zig-zag pattern of dielectric marked by yellow. (b) Transmission and reflection spectra for a vertical U-turn bends in the square spiral based 3D circuits. The length of vertical interconnect is $3.75c$.

pores, and square spiral 3D PBG materials. Single-mode waveguiding in air is obtained over a large bandwidth of up to 200 nm within planar micro-chip layers and 100 nm for chip-to-chip interconnects. In particular, a 'U-turn' circuit path connecting two adjacent micro-chip layers is optimized to yield high transmission over the entire waveguiding bandwidth. We have suggested that the vertical U-turn and the in-plane (x-y) $90°$ waveguide bend provide the building blocks for more complex 3D, non-planar, optical circuit paths. The 2D micro-chip circuit paths may contain coupling to micro-cavities, T-junctions, and cross-connects as shown earlier for idealized 2D photonic crystals [6]. High-bandwidth optical circuitry written into a 3D PBG microchip combined with novel active devices on-chip [39], may provide unprecedented compactness, information density, and processing speed for future optical communications and computing. In this regard, the design of optical isolators [40] for the 3D PBG micro-chip may be very important to prevent unwanted wave-interference effects between different devices placed along a long circuit path. The realization of these far-reaching goals requires careful and accurate materials fabrication methods. One such approach, using direct laser writing of PBG architectures [41, 42] in a polymer photoresist followed by replication with a high index semiconductor such as silicon [43] is already underway [44].

Appendix: mode structure and degeneracy of 3D PBG cladding

In this Appendix, we provide a simple physical interpretation of the degeneracy of the four lowest bands of the 3D woodpile structure at the Z-point of the Brillouin zone boundary. The understanding of these electromagnetic mode field patterns plays an essential role in the design of the vertical wave-guide interconnect between planar micro-chip layers. First, consider the modes that are polarized along the y-direction at the Brillouin zone boundary. We refer to these as the first and the third bands. For the first band, the amplitude of the electric field at positions along the z-direction is qualitatively described in Fig. 12, where the $+$, $-$ signs represent positive and negative values, respectively. We denote the mode structure of the first band as $++--++--$. Note that the Bloch wave vector at the Z-point is π/c. In other words, the period of the EM wave in the first band at Z is $2c$. For the third band, there exists an additional superimposed oscillation of wave vector $2\pi/c$, corresponding to $+-+-+-+-$. Multiplying this to the field amplitude of the first band, we obtain the field amplitude for the third band as $+--++--+$. This is precisely the field of the first band with a phase shift of $\pi/2$. Given symmetry between the first and the third layers of the woodpile structure, it follows
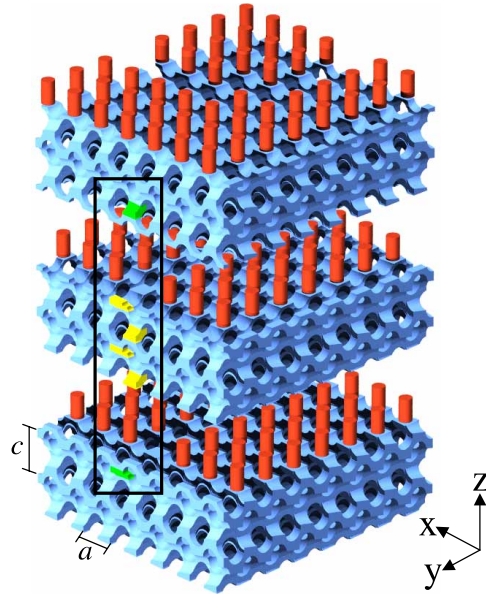
Fig. 11. Schematic of the 3+1D optical micro-chip using the inverse square spiral 3D PBG architecture. The bottom, second, and third cladding sections of the micro-chip (consisting of the inverse square spiral 3D PBG material) are separated to help visualize the 2D micro-chip layers. (The topmost cladding section is not shown). The vertical waveguide, connecting the bottom and the second micro-chip layers, is created by removing a zig-zag pattern of dielectric rods along the *y*-direction marked by yellow and green. This pattern of removed dielectric is the same as for the U-turn interconnects of the woodpile based 3+1D circuits shown in Fig. 1(a) and that of the **SP₂** based 3+1D circuits shown in Fig. 7. The left surface showing the vertical waveguide (highlighted with black wire frame) corresponds to the cross-section *y*=0.7*a* (see Fig. 10(a)).
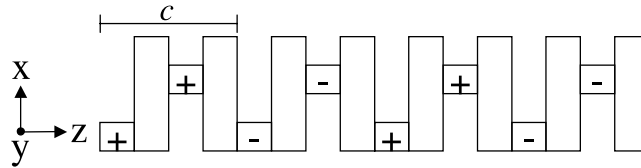

Fig. 12. Schematic describing electric field amplitude at positions along the *z*-direction for the first band of the woodpile structure. The Bloch vector is equal to π/c. The $+, -$ signs represent positive and negative values, respectively.

that the first and third bands are degenerate at the Brillouin zone boundary. The degeneracy between the first and second bands is a direct consequence of the symmetry of the structure between the *x*- and *y*- directions. The second and fourth bands are related to each other by a $\pi/2$ phase shift as described above.

Acknowledgements